Intrinsic Oceanic Decadal Variability of Upper-Ocean Heat Content

NAVID C. CONSTANTINOU[a] AND ANDREW MCC. HOGG[a]

[a] Research School of Earth Sciences and ARC Centre of Excellence for Climate Extremes, Australian National University,
Canberra, Australian Capital Territory, Australia

ABSTRACT: Atmosphere and ocean are coupled via air–sea interactions. The atmospheric conditions fuel the ocean circulation and its variability, but the extent to which ocean processes can affect the atmosphere at decadal time scales remains unclear. In particular, such low-frequency variability is difficult to extract from the short observational record, meaning that climate models are the primary tools deployed to resolve this question. Here, we assess how the ocean's intrinsic variability leads to patterns of upper-ocean heat content that vary at decadal time scales. These patterns have the potential to feed back on the atmosphere and thereby affect climate modes of variability, such as El Niño or the interdecadal Pacific oscillation. We use the output from a global ocean–sea ice circulation model at three different horizontal resolutions, each driven by the same atmospheric reanalysis. To disentangle the variability of the ocean's direct response to atmospheric forcing from the variability due to intrinsic ocean dynamics, we compare model runs driven with interannually varying forcing (1958–2018) and model runs driven with repeat-year forcing. Models with coarse resolution that rely on eddy parameterizations show (i) significantly reduced variance of the upper-ocean heat content at decadal time scales and (ii) differences in the spatial patterns of low-frequency variability compared with higher-resolution models. Climate projections are typically done with general circulation models with coarse-resolution ocean components. Therefore, these biases affect our ability to predict decadal climate modes of variability and, in turn, hinder climate projections. Our results suggest that for improving climate projections, the community should move toward coupled climate models with higher oceanic resolution.

KEYWORDS: Eddies; Mesoscale processes; Ocean circulation; Atmosphere-ocean interaction; Empirical orthogonal functions; Principal components analysis; Model comparison; Climate variability; Decadal variability; Oceanic variability

1. Introduction

The atmosphere and ocean communicate at the sea surface via air–sea interactions allowing the exchange of heat, freshwater, and momentum. There is clear evidence that the atmosphere affects the ocean, since it is responsible for setting up the wind stress and the meridional buoyancy gradients that fuel the ocean's mean circulation and its variability. At high frequencies (~weekly), the atmosphere's synoptic variability appears at large length scales (~1000 km). The ocean's large heat capacity acts as memory since it results in suppressing or "integrating out" the high-frequency atmospheric variability, enhancing power on longer time scales (~decadal) of the coupled atmosphere–ocean climate system. This is the "null hypothesis" for explaining the observed red spectrum of the climate variability. According to the null hypothesis, the ocean's low-frequency response results solely from the atmosphere's high-frequency synoptic variability (which, from the ocean's viewpoint, appears to leading order as stochastic excitation), and the role of the ocean is to introduce the slower time scale (due to its larger heat capacity) so that the atmosphere's stochastic nudging becomes a red-noise process inducing power at low frequencies (Hasselmann 1976; Frankignoul and Hasselmann 1977). The null-hypothesis paradigm forms the basis of many air–sea coupling studies up to date (e.g., Barsugli and Battisti 1998).

Recent work revealed that the null-hypothesis paradigm is only one part of the story. It has been shown that the variability of air–sea heat fluxes over ocean regions outside the tropics with high mesoscale eddy activity shows a different character from the null-hypothesis prediction: air–sea heat fluxes are not predominantly controlled by the atmosphere in those regions, but rather the other way around (Bryan et al. 2010; Buckley et al. 2014, 2015; Bishop et al. 2017; Small et al. 2019, 2020). The question remains whether the ocean's *intrinsic variability* can enhance power at interannual frequencies, thus allowing for the potential to affect the climate at decadal time scales.[1] Is it possible that the ocean's variability can enhance the low-frequency variability of air–sea heat fluxes through the ocean's capacity to create sea surface temperature variability at decadal time scales? Furthermore, to what extent does such low-frequency variability affect the atmosphere (Vallis 2010)? We attempt here to tackle both of these questions. Thus, our main objective in this paper is to assess whether and how the ocean's intrinsic variability affects the climate variability on decadal time scales.

What could be the cause of such ocean-generated decadal variability? One hypothesis is that the high-frequency atmospheric variability acts as noise, thus enabling the ocean to undergo transitions between different close-to-equilibrium states. Take, for example, a particle in a double-well potential. Without any external noise the particle sits at the bottom of either of the potential wells. With some noise, the particle starts wandering around the bottom of the well and, when the

---

[1] By "intrinsic ocean variability" here, we mean the variability that rises due to oceanic dynamical processes and not as a direct response of the ocean to the atmospheric forcing; we will refer to the latter as "forced ocean variability."

noise becomes sufficiently strong, the particle may jump between wells and end up at the bottom of the neighboring potential well. Such transitions from one well to another occur less frequently than oscillations due to noise and thus appear as low-frequency variability of the particle's position. Turbulent flows often support large-scale coherent features; such features are ubiquitous in the ocean (e.g., the Gulf Stream, Kuroshio, and Antarctic Circumpolar Current). The different states of these coherent features manifest as equilibria of the dynamics that the flow statistics obey (e.g., Farrell and Ioannou 2008; Parker and Krommes 2013; Constantinou et al. 2014; Constantinou 2015; Farrell and Ioannou 2019). In general, flows tend to "wander around" such equilibria (similarly to how the particle wanders around the bottom of the well when there is noise). When the turbulent flow attractor possesses more than one stable equilibrium (i.e., exhibits "bistability" with a double well), then transitions between such equilibria can occur (Kimoto and Ghil 1993; Qiu and Miao 2000; Pierini 2006; Pierini et al. 2009; Parker and Krommes 2013; Constantinou 2015). These transitions typically occur at much longer time scales than the time scale the flow exhibits and, thus, appear as lower-frequency variability.

In the atmosphere, low-frequency variability of precisely this character was demonstrated with the seminal experiments by James and James (1992). Those experiments revealed a so-called ultra-low-frequency variability, which was shown to come about from transitions between a two-jet state, with a subtropical jet distinct from an eddy-driven midlatitude jet, and a single or merged jet state. Therefore, in James and James's (1992) experiments, the intrinsic nonlinearity of the atmosphere became the source of low-frequency variability. Notably, James (1998) argued that models with parameterizations cannot capture the low-frequency variability that was seen in the experiments of James and James (1992). Recent studies demonstrated the occurrence of intrinsic low-frequency variability due to bistability of the turbulent attractor in barotropic models (Bouchet et al. 2019; Simonnet et al. 2021).

In the ocean, the primary patterns of variability occur on smaller scales (~100 km) and lower frequencies (~months) than the atmosphere, through the creation of mesoscale eddies predominantly via baroclinic instability. However, the influence of nonlinear processes in creating *intrinsic* variability at lower frequencies (defined in this paper to be approximately decadal) is difficult to evaluate either from observations or coupled climate models, because variability of the ocean circulation is also *forced* from the atmosphere. The superposition of forced and intrinsic variability requires a targeted approach to the problem.

Hogg et al. (2005) found that idealized eddy-rich ocean models show high intrinsic variability, which is greatest in eddying regions and can influence the atmospheric variability (see also Hogg et al. 2006; Martin et al. 2020, 2021). Bistability in the oceanographic context has been discussed by Deshayes et al. (2013) and Aoki et al. (2020). Other mechanistic and dynamical explanations have been proposed as candidates for inducing low-frequency variability in the ocean: the turbulent oscillator (Berloff et al. 2007), which involves eddy–mean flow

feedback between meridional eddy fluxes and the strength of a quasi-zonal jet. These proposed mechanisms depend largely on resolving nonlinear scales of motion, principally ocean eddies. Climate projections, on the other hand, are routinely done with general circulation models that use a "laminar ocean," that is, ocean components whose lateral resolution is too coarse to resolve ocean eddies and instead rely on eddy parameterizations (Hewitt et al. 2020). What remains outstanding and forms the basic question addressed in this paper is whether the ocean's intrinsic mesoscale flow has the potential to affect the large-scale patterns of sea surface temperature variability at decadal time scales.

A series of studies aimed to better understand the forced and intrinsic response of the ocean using numerical experiments utilized a large ensemble of global ocean–sea ice model simulations (OCCIPUT project; http://meom-group.github.io/projects/occiput). These simulations were all initialized with slightly different initial conditions and they were run at a resolution that was able to partially resolve some of the ocean eddies (Penduff et al. 2011). The chaotic nature of the ocean's intrinsic variability in certain regions led to a spread in the solutions, while in other regions where the forced component dominates, the oceanic response among the ensemble members revealed more similarities. These results suggested that intrinsic low-frequency variability is significant in eddy-present models and can be as large as 80% of all observed variability in regions of high ocean-eddy activity (see also Penduff et al. 2018; Leroux et al. 2018). Sérazin et al. (2017) used the OCCIPUT ensemble dataset to quantify the forced and intrinsic footprint of the ocean heat content at decadal time scales. They found that the ocean heat content variance at decadal time scales increased in regions of high eddy activity. Here, we will focus on the upper-ocean heat content and study how low-frequency variance changes as we go from models that parameterize ocean eddies toward models that resolve the eddies. We furthermore determine the main patterns of low-frequency intrinsic variability that ocean dynamics induce on the upper-ocean heat content using an empirical orthogonal function (EOF) analysis and study how these patterns change with increasing model resolution.

One approach to decompose forced from intrinsic ocean variability is to use long, eddy-rich global ocean–sea ice model runs (Sérazin et al. 2015). To distinguish the forced from the intrinsic component, we can compare ocean–sea ice models driven by realistic, interannually varying atmospheric forcing with models driven by a modified atmospheric forcing that does not vary at subannual frequencies (Stewart et al. 2020). Given that in the latter experiments the forcing of the models is repeated every year, and thus does not vary at time scales longer than one year, any ocean variability we observe at decadal time scales is attributed to intrinsic variability. In this paper, we will undertake this approach to disentangle the forced from the intrinsic ocean's response, and also to compare how the intrinsic variability of the upper-ocean heat content varies as we refine our model's lateral resolution to better resolve ocean eddies.

In what follows, we describe in detail the datasets we use and the methods we apply to understand the low-frequency variability of upper-ocean heat content (section 2). Our results are

TABLE 1. Record length and time period of the satellite altimetry observational dataset by the Copernicus Marine and Environment Monitoring Service (CMEMS) and model output used in this study. Simulations are indicated by their resolution (1°, 0.25°, or 0.1°) and forcing method (IAF = interannual forcing; RYF = repeat-year forcing).

Abbreviation		Period of forcing	Record length (yr)	Frequency
CMEMS	(satellite)	Jan 1993–Dec 2019	27	Monthly
IAF 1°	JRA55-do v1.3	Jan 1958–Dec 2017	240 (4 cycles)	Yearly UOHC, monthly SSH
IAF 0.25°	JRA55-do v1.3	Jan 1958–Dec 2017	258 (>4 cycles)	Yearly UOHC, monthly SSH
IAF 0.10°	JRA55-do v1.4	Jan 1958–Dec 2018	183 (3 cycles)	Monthly
RYF 1°	JRA55-do v1.3	May 1990–Apr 1991	260	Monthly
RYF 0.25°	JRA55-do v1.3	May 1990–Apr 1991	250	Monthly
RYF 0.10°	JRA55-do v1.3	May 1990–Apr 1991	220	Monthly

then presented in section 3, which is partitioned in two parts: section 3a studies the intrinsic versus forced low-frequency variance content across models with different lateral resolutions and section 3b presents global and regional EOF analysis to understand the main modes of spatial and temporal low-frequency variability. We conclude with a discussion in section 4.

2. Methods

We use the ocean–sea ice model ACCESS-OM2 at three different horizontal resolutions (Kiss et al. 2020): eddy-rich at 0.10°, eddy-present at 0.25°, and at 1° with parameterized eddies.[2] The model is forced with 3-hourly output from the atmospheric reanalysis JRA55-do dataset (Tsujino et al. 2018). To separate the intrinsic from the forced component of the oceanic flow, we use two different forcing strategies: (i) 3-hourly interannually varying forcing (IAF) from 1958 to 2018, which is repeated to yield multiple ~60-yr cycles, and (ii) 3-hourly repeat-year forcing (RYF), defined to be time-varying forcing from a single year (May 1990–April 1991; in which major climate mode indices are neutral) that keeps repeating itself (Stewart et al. 2020). Note that the IAF cycles are combined together in one long time series for analysis. None of the RYF forcing fields used to drive the ocean has power at time scales longer than one year. Thus, in RYF experiments, any variability at time scales longer than one year is attributed to intrinsic oceanic processes. More details about the datasets used here, including the length of the model runs, are reported in Table 1.

The atmosphere feels the ocean primarily as a thermal boundary condition and, thus, one may argue that to quantify the effect of how the ocean feeds back on the atmosphere, we should look at sea surface temperature. However, in ocean–sea ice models, such as that used here, the prescribed atmosphere does not respond to oceanic heat fluxes. Therefore, the atmosphere has effectively infinite heat capacity and the sea surface temperature is, to a large degree, "slaved" to the imposed

atmospheric state (Hyder et al. 2018). The nature of this forcing complicates how we can disentangle the forced from the intrinsic oceanic response. To overcome this impasse, we will use two other flow quantities to quantify the ocean's feedback back to the atmosphere and the global climate at decadal time scales: the sea surface height (SSH) and the upper-ocean heat content (e.g., conservative temperature) integrated over, say, the top 50 m of the ocean. By integrating over the top 50 m of the ocean, we alleviate the "slaving" effect of the sea surface temperature to the forcing fields that drive the model.

The sea surface height is intimately related to (albeit not a direct measure of) upper-ocean heat content. But more importantly, the observational satellite altimetry record since 1993 allows an estimate of the low-frequency variability from observations, which can be used to ground truth the models. Of course, the observational altimetry record is short (27 years) and, therefore, one should be cautious while interpreting estimates of variability at decadal time scales or longer from such a short record. However, comparison with observations enables us to evaluate how well the model captures variability at time scales shorter than 27 years.

In summary, we use output from models with 1°, 0.25°, and 0.10° horizontal resolution and also the sea surface height observations from the gridded altimetry [Copernicus Marine and Environment Monitoring Service (CMEMS)] dataset at 0.25° resolution. We first interpolate *all* flow fields to a a regular longitude and latitude grid with horizontal resolution of 1°. The motivation behind this choice is that we want to coarsen the resolution to a common grid, so that the baseline resolution of the data processing is equivalent.

The upper-ocean heat content $\mathcal{H}$ is taken, here, as the heat content over the top 50 m of the ocean:

$$\mathcal{H}(\text{lon}, \text{lat}, t) = \rho_0 c_p \int_{-50\text{m}}^{\eta} T(\text{lon}, \text{lat}, z, t)\, dz, \quad (1)$$

where T is the conservative temperature from the model, η is the sea surface height, $\rho_0 = 1035.0 \text{ kg m}^{-3}$ is the mean density of seawater, and $c_p = 3992.1 \text{ J K}^{-1} \text{ kg}^{-1}$ is the specific heat capacity of seawater. The choice of defining upper-ocean heat content over the first 50 m of the ocean may seem arbitrary; a more natural definition would be to define the upper-ocean heat content over the mixed-layer depth. However, such a

---

[2] Note that so-called eddy-present/eddy-rich characterizations do not derive from any strict definition. We use them here implying that an eddy-rich model resolves eddies at most latitudes, while an eddy-present model only resolves eddies in the tropics (Hallberg 2013; Hewitt et al. 2020).

mixed-layer-depth-dependent definition would create difficulties for comparing across different models with differing lateral resolution and mixed-layer biases. We therefore choose a fixed depth for defining upper-ocean heat content and keep in mind that this may result in an underestimate of upper-ocean heat content for regions where the mixed layer is deeper, and an overestimate of upper-ocean heat content in regions where the mixed layer is shallower.

After coarsening all flow fields, we proceed with a frequency decomposition. For example, the upper-ocean heat content is decomposed in frequencies via a Fourier transform as

$$\hat{\mathcal{H}}(\mathrm{lon,lat},f) = \int \mathcal{H}(\mathrm{lon,lat},t)e^{-2\pi i f t}\,dt. \quad (2)$$

We denote the low-frequency component to be anything that corresponds to frequencies smaller than $f_{max} = (1.5\,\mathrm{yr})^{-1}$ (to ensure we exclude the dominant peak of the seasonal cycle) and also larger than a low-frequency cutoff f_{min}; that is,

$$\hat{\mathcal{H}}_{LF} = \begin{cases} \hat{\mathcal{H}} & \text{if } f_{min} < f < f_{max}, \\ 0 & \text{otherwise}. \end{cases} \quad (3)$$

The lower-frequency cutoff f_{min} in Eq. (3) is chosen to be small enough to include decadal time scales, while excluding any long-term model drift. Given that we also want to compare with the satellite altimetry record (which is only 27 years long), we choose $f_{min} = (25\,\mathrm{yr})^{-1}$.

We can reconstruct the low-frequency component of our signal via an inverse Fourier transform of the frequency decomposition in Eq. (3):

$$\mathcal{H}_{LF} = \int \hat{\mathcal{H}}_{LF}\,e^{2\pi i f t}\,df. \quad (4)$$

In view of Parseval's theorem, the low-frequency variance is then given by

$$\mathrm{var}[\mathcal{H}_{LF}](\mathrm{lon,lat}) = \frac{1}{\Delta t}\int \mathcal{H}_{LF}^2\,dt = \frac{1}{\Delta t}\int_{f_{min}}^{f_{max}} |\hat{\mathcal{H}}_{LF}|^2\,df, \quad (5)$$

where Δt is the duration of the time series of the signal. Similar frequency decomposition and quantification of the low-frequency variance as in Eqs. (2), (3), and (5) is also performed for the sea surface height as obtained both from model output and from observations, yielding an estimate of var[SSH_{LF}]. To identify the spatial and temporal patterns of variability, we perform EOF analysis on the low-frequency component of upper-ocean heat content $\mathcal{H}_{LF}$.

3. Results

a. Low-frequency variability

We first look into the low-frequency variability of sea surface height and compare it across models with interannual or repeat-year forcing, and across the three horizontal resolutions. As discussed above, although sea surface height is not a direct measure of the thermal forcing that the ocean feeds back to the atmosphere, the observed satellite altimetry record can provide a ground truth for the interannually forced model.

Figure 1 shows maps of the low-frequency variance for sea surface height [see Eq. (5)]. Figures 1a, 1d, and 1g show the results from the interannually forced models at the three different resolutions while Fig. 1j shows the same map obtained from satellite altimetry (CMEMS). The low-frequency variance in the interannually forced model at high resolution (Fig. 1g) resembles that in the observations (Fig. 1j); Fig. 1k shows the ratio of the IAF 0.10° variance over observations (for the period 1993–2018), demonstrating that in most of extratropical regions the model captures at least 80% of the low-frequency variance seen in observations. Close inspection of the ratio in Fig. 1k reveals that the regions where low-frequency variance differs between model and observations are in the tropical Pacific and Indian Ocean, and the extension of the Kuroshio east of Japan. The tropical Indo–Pacific is dominated by interannual variability [El Niño–Southern Oscillation (ENSO) and the Indian Ocean dipole (IOD)], which depends on coupled ocean–atmosphere dynamics (Webster et al. 1999; Timmermann et al. 2018); therefore, weaker variability in this region is expected in an ocean-only simulation. Regarding the Kuroshio Extension region, it has been documented that the Kuroshio undergoes decadal transitions between two different states (Qiu and Chen 2010) and the variance associated with these transitions requires a longer observational record to be accurately captured.

Comparison of the IAF simulations at the three different resolutions (Figs. 1a,d,g) shows that, on one hand, the low-frequency variance in the tropics seems insensitive to increasing resolution, while on the other hand, midlatitude and eddy-rich regions (like the Southern Ocean, the Kuroshio, the Gulf Stream, and their extensions) show progressively more low-frequency variance as we increase the model resolution. Remember that flow fields from models across all resolutions have been interpolated to a grid with nominal 1° spacing and, therefore, the increased extratropical variance of Fig. 1g compared with Fig. 1a suggests that the model resolution affects the large-scale, low-frequency patterns of variability for the eddy-rich model, when compared with the eddy-present model. The insensitivity of the low-frequency variance in the tropics to model resolution may occur because variability in that region is dominated by atmospheric interaction, or because eddies, tropical instability waves, and large-scale Kelvin waves, which come into play in the tropics and in particular in the tropical Pacific, are partially resolved even at the coarse 1° resolution.

Oceanic eddies are generated intrinsically from oceanic processes (baroclinic or barotropic instability of currents, bathymetry interactions) and these processes are particularly active in the midlatitudes. Thus, one would logically hypothesize that oceanic eddies are likely to contribute to increased variance at these latitudes. However, eddies occur on time scales less than a year, so the observed increase in *low-frequency* variance between the 1° IAF model (Fig. 1a) and the 0.10° IAF model (Fig. 1g) cannot be explained by the direct effect of ocean eddies.

To better understand the contribution of the intrinsic oceanic response to the atmospheric forcing, and how that leads to decadal patterns of variability, we turn next to the repeat-year
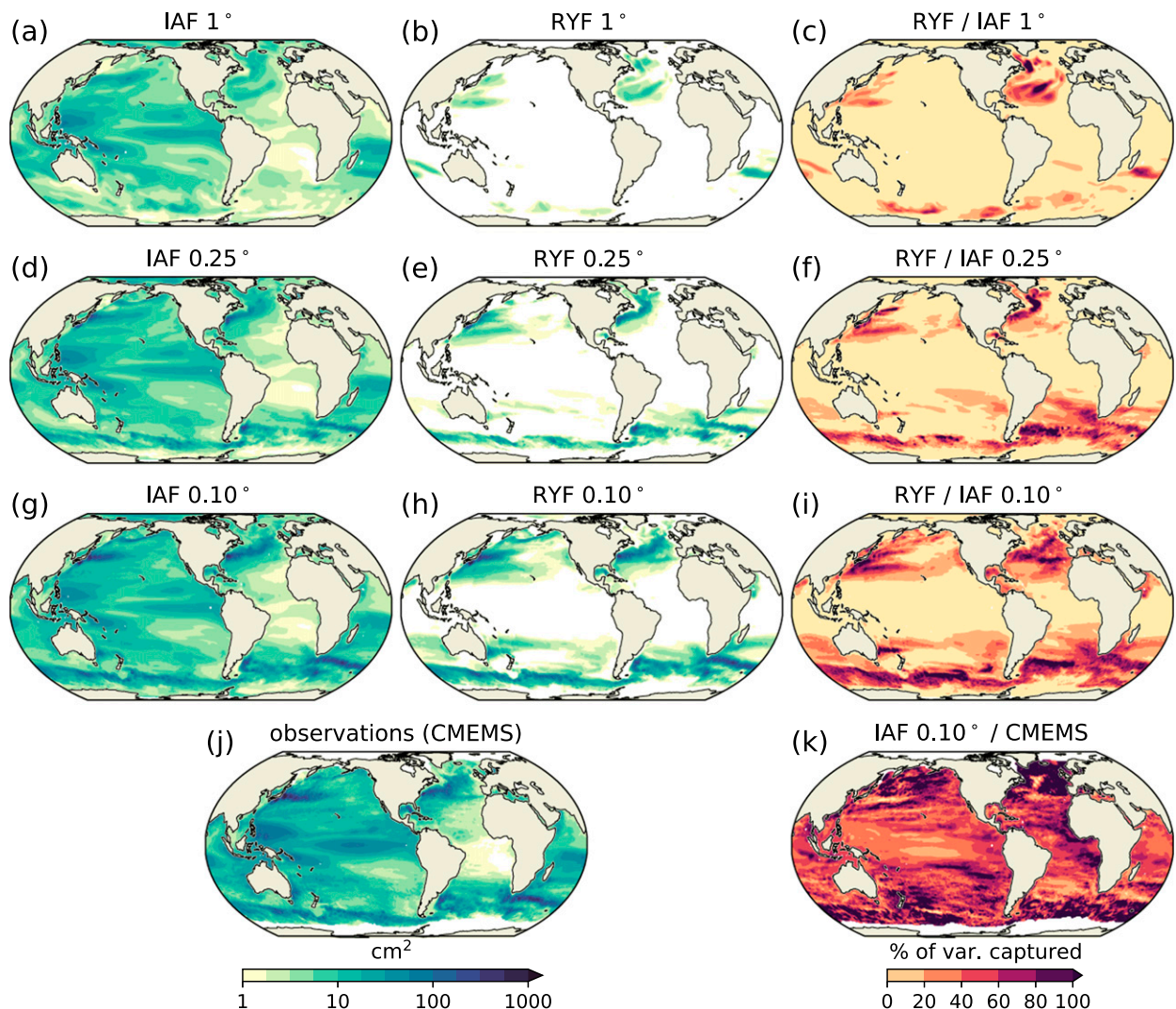
FIG. 1. Sea surface height (SSH) low-frequency variance, var[SSH$_{LF}$] [frequencies between $(25\,\mathrm{yr})^{-1}$ and $(1.5\,\mathrm{yr})^{-1}$] from ACCESS-OM2 models at three different resolutions and from satellite altimetry (CMEMS). (a),(d),(g) Models forced with interannually varying forcing (IAF) from the JRA55-do dataset during 1958–2018; (b),(e),(h) models forced with repeat-year forcing (RYF) from the JRA55-do dataset; (j) results from observations. (c),(f),(i) Ratio of the RYF over the IAF low-frequency variance at the corresponding model resolution; (k) ratio of the low-frequency variance in observations over that from the IAF model at 0.10° for the same period. (Only data between 65°S and 65°N were used from the CMEMS dataset.)

forcing model runs. The corresponding maps of the integrated low-frequency variance for sea surface height for RYF models are shown in Figs. 1b, 1e, and 1h. The striking difference compared with the IAF model runs is the lack of low-frequency variance at the tropics. This lack of tropical low-frequency variability in the RYF runs implies that low-frequency variability in the tropics is dominated by atmospheric interactions (e.g., ENSO), and accounts for the insensitivity of tropical variability to resolution in the IAF simulations. On the other hand, the RYF models show significant low-frequency variance in the extratropical regions that increases with model resolution (cf. Figs. 1b, 1e, and 1h). This variance is attributed to intrinsic oceanic variability.

One can ask how much of the total low-frequency variance is due to intrinsic processes and how much is due to the low-frequency component of the forcing. Assuming that the IAF runs represent low-frequency variance resulting from both intrinsic and forced motions, then the ratio of the low-frequency content variance from RYF over that from IAF (Figs. 1c, 1f, and 1i, respectively) depicts the percentage of intrinsic low-frequency variance in each model resolution. Two things should be taken away from Figs. 1c, 1f, and 1i: that the percentage of intrinsic variance increases with model resolution, and that the regions of intrinsic low-frequency variance in models with parameterized eddies differ from those seen in the eddy-rich models.
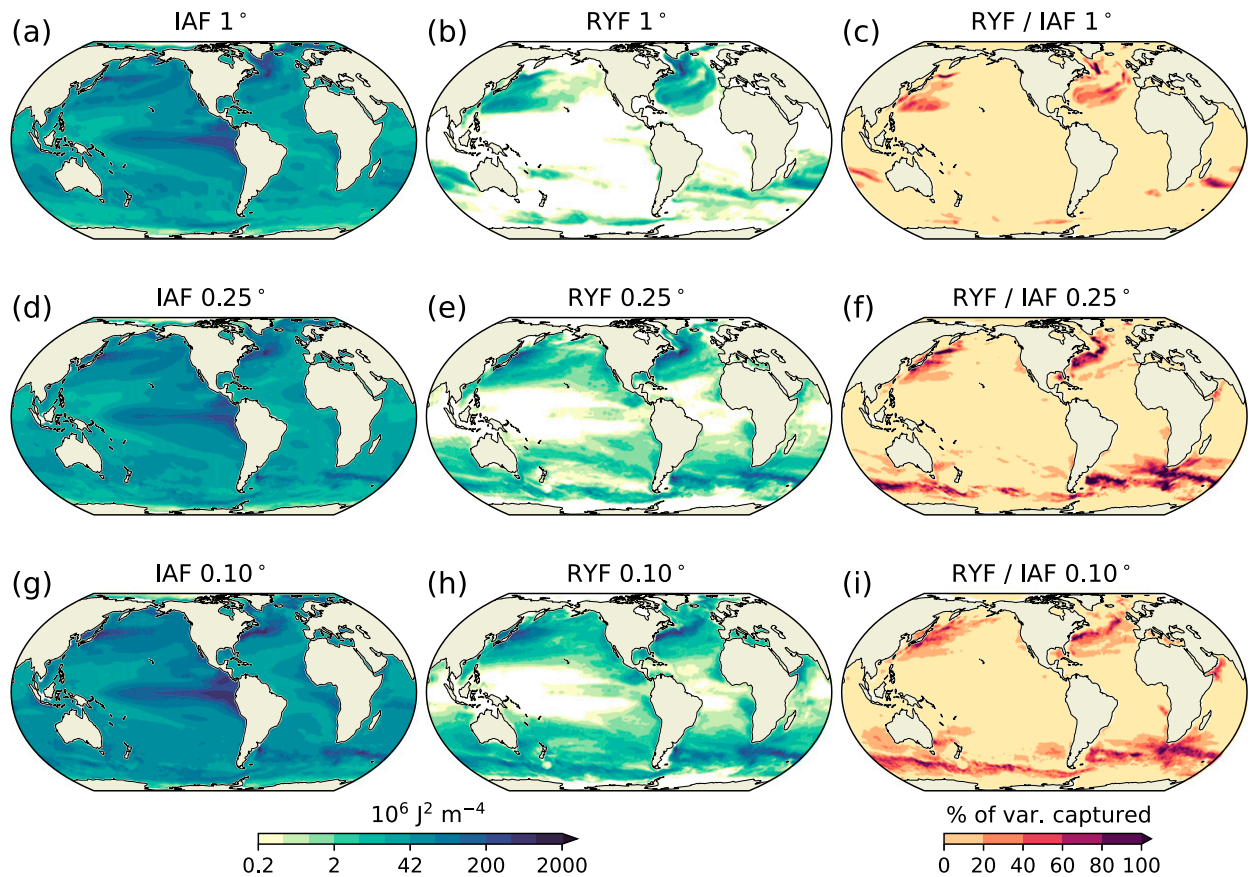
FIG. 2. Upper-ocean heat content (top 50 m) low-frequency variance, var[$\mathcal{H}_{LF}$] [frequencies between $(25\,\mathrm{yr})^{-1}$ and $(1.5\,\mathrm{yr})^{-1}$] from ACCESS-OM2 models at three different resolutions. (a),(d),(g) Models forced with interannually varying forcing (IAF) from the JRA55-do dataset during 1958–2018; (b),(e),(h) models forced with repeat-year forcing (RYF) from the JRA55-do dataset; (c),(f),(i) ratio of the RYF over the IAF frequency content at the corresponding model resolution.

The analysis of the sea surface height above demonstrates that (i) the IAF models, at least at the eddy-rich 0.10° resolution, adequately capture the variance seen in the observational record from satellite altimetry (Fig. 1k), and (ii) that intrinsic low-frequency variance is enhanced when oceanic eddies are resolved. Point (i) allows us to trust that our model captures the phenomena we are trying to assess, while point (ii) suggests that this analysis is worthy of further investigation. We turn now to the upper-ocean heat content, a quantity that may directly influence the atmosphere.

Figure 2 shows maps of the integrated low-frequency variance for upper-ocean heat content (in a similar manner as seen in Fig. 1 for sea surface height, but without any comparison to observations). The results are similar to those seen in the sea surface height analysis of Fig. 1: intrinsic low-frequency variance increases with model resolution outside the tropics, while low-frequency variance within the tropics only appears in IAF model runs and is insensitive to model resolution. Furthermore, for the eddy-rich 0.10° resolution, Fig. 2i suggests that in the eddy-rich regions, more than 50% of the low-frequency variance is due to intrinsic oceanic variability.

In both sea surface height and upper-ocean heat content analyses, we note enhanced low-frequency variance in the North Atlantic, and in particular in the Labrador Sea, for the coarse 1°-resolution model runs. This enhanced variance can be seen both in the IAF and RYF models (see Figs. 1a,b and 2a,b) but it is not apparent in eddy-rich model runs nor in the sea surface height observations of Fig. 1j. This variability occurs because of spurious convection that occurs in the Labrador Sea in models with parameterized eddies (Ortega et al. 2017). The enhanced low-frequency variance that shows up in the Labrador Sea in 1° models is replaced by variance in the North Atlantic region at the location of the Gulf Stream Extension in the 0.10° model.

b. Spatial and temporal patterns of large-scale low-frequency variability

We have established that intrinsic oceanic variability leads to enhanced low-frequency patterns of upper-ocean heat content. But maps like those in Figs. 1 and 2 only quantify the variance and do not elaborate on the spatial or temporal patterns of the low-frequency signal that the atmosphere may feel
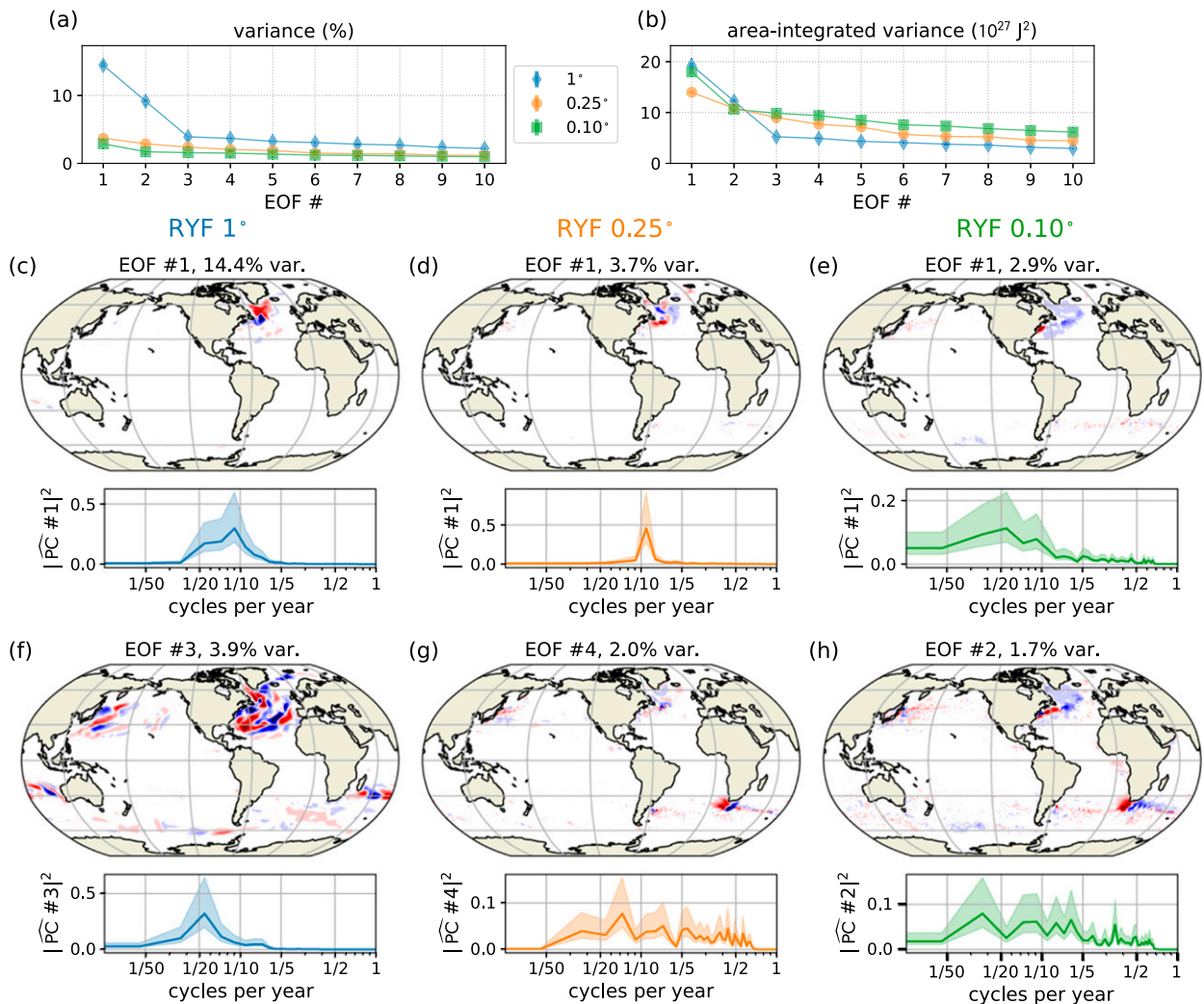
Global EOF analysis

FIG. 3. Global EOF analysis of the low-frequency reconstructed upper-ocean heat content $\mathcal{H}_{LF}$ [see Eq. (4)] for models driven by repeat-year forcing at 1°, 0.25°, and 0.10° resolutions. (a),(b) Percentage and the area-integrated explained variance for the first 10 EOFs. (c)–(e) (top) The first EOF for each model resolution; (f)–(h) (top) another EOF, selected to emphasize a mode that is qualitatively different from EOF1. (c)–(h) (bottom) the spatial structure of the EOF and the frequency power spectrum of the principal component (PC) time series of the corresponding EOF. Contours for the EOF maps in (c)–(h) are saturated at values $\pm(1/2)\max|\text{EOF}|$.

as a result of the ocean's intrinsic variability. To better understand and quantify the spatial and temporal patterns of low-frequency intrinsic oceanic variability, we perform an EOF analysis on the low-frequency reconstruction of the upper-ocean heat content, $\mathcal{H}_{LF}$ [see Eq. (4)] from the RYF model output. Details on error bars and sensitivity checks of the EOF-analysis are provided in the appendix.

Figure 3 shows the global EOF analysis of the low-frequency upper-ocean heat content. Figure 3a shows the percentage of the total low-frequency variance explained for each EOF and for each model resolution, while Fig. 3b shows the total variance explained for each EOF for each model resolution. Note that output from different model resolutions has been interpolated

onto a grid of 1° nominal resolution. Therefore, the higher variance at increased resolution is not a direct effect of oceanic eddies. This result reiterates once more that models that resolve ocean eddies present enhanced large-scale, low-frequency variance of the upper-ocean heat content. The spatial patterns that emerge (Figs. 3c–h) are associated with the regions of enhanced variance seen in Figs. 2b, 2e, and 2h. Note that the EOF patterns from the 0.1° model (Figs. 3e,h) resemble features associated with regions of high eddy activity.

The global EOF analyses in Fig. 3 are dominated by patterns of limited spatial extent. It follows that independent processes act in different ocean basins meaning that we can refine our understanding of these individual processes by limiting the
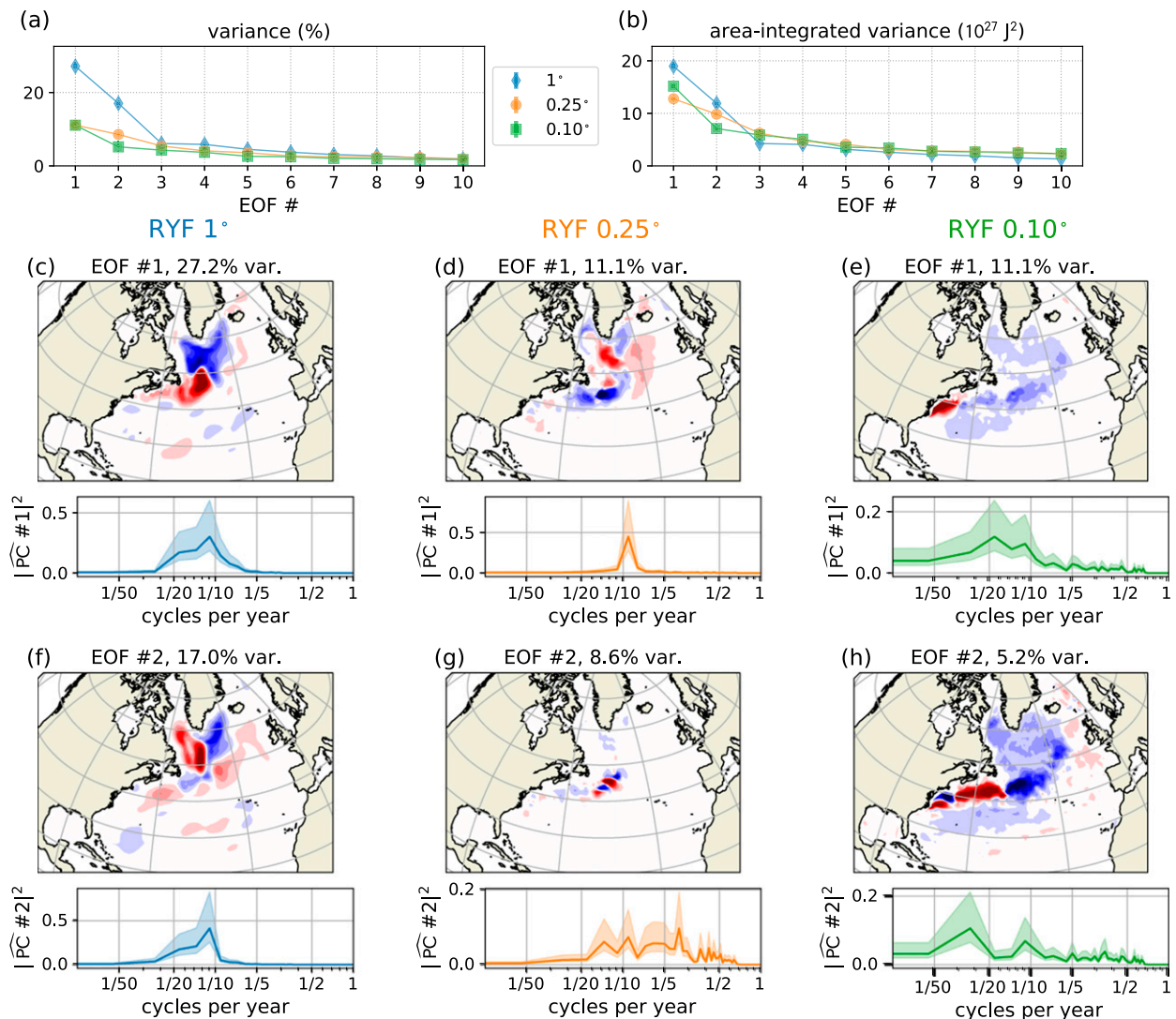
FIG. 4. Regional EOF analysis for the North Atlantic Ocean (20°–75°N, 100°–0°W). (a),(b) Percentage and the area-integrated explained variance for the first 10 EOFs over the region. (c)–(h) (top) The spatial structure of the EOF and the frequency power spectrum of the principal component (PC) time series of the corresponding EOF and (bottom) the first EOF for each model resolution and also an additional EOF selected to emphasize a mode that is qualitatively different from EOF1. Contours for the EOF maps in (c)–(j) are saturated at values ±(1/2)max|EOF|.

regional extent of these EOF analyses. Thus, we next perform regional EOF analyses in the North Atlantic, the North Pacific, the Indian Ocean, and the South Atlantic regions (see Figs. 4–7 respectively). A feature that emerges from all EOF patterns is that, with increasing model resolution the patterns of low-frequency variability become more aligned with the eddy-rich regions (e.g., the western boundary currents and their extensions and the Southern Ocean). In terms of low-frequency sea surface height variance, the highest-resolution models showed better agreement with observations compared to coarse-resolution models (see Figs. 1a,d,g,j). This result implies that the patterns concentrated in eddy-rich regions that were

revealed by the EOF analysis for 0.10° resolution models are closer to reality compared with 1° resolution models.

In the North Atlantic, the 1° model shows more low-frequency variance than the higher-resolution models. The variance in the 1° model occurs in the Labrador Sea (Figs. 4c,f) and it is intimately related to the spurious numerical convection that occurs there. We note that the signature of Labrador Sea spurious convection (Figs. 4c,f) is almost completely eliminated in the eddy-rich 0.10° model (Figs. 4e,h), which shows low-frequency variance at the location of the Gulf Stream and its extension. The leading EOF of the eddy-present model (RYF 0.25°) appears as a combination of the other two,
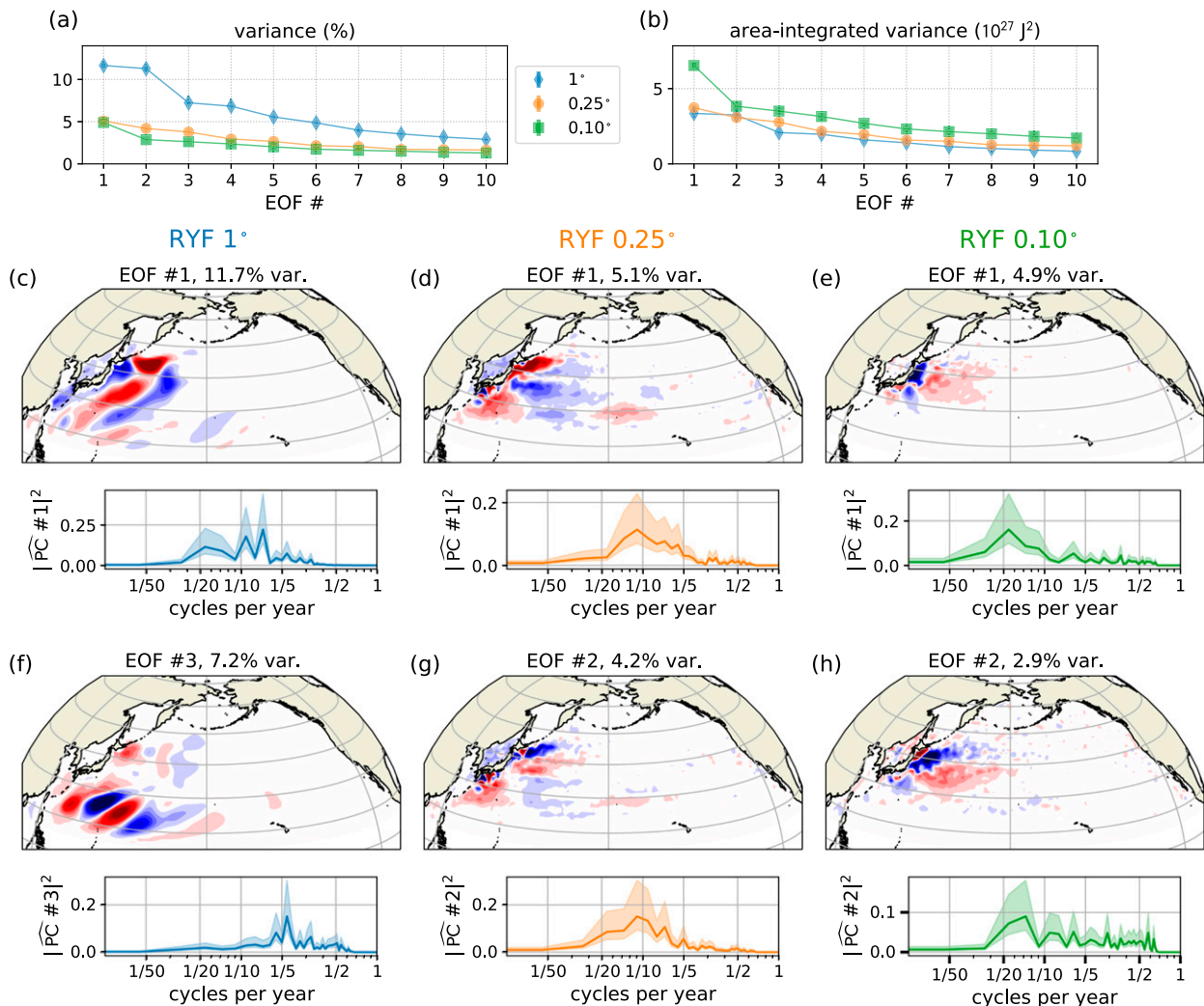
EOF analysis of North Pacific

FIG. 5. Regional EOF analysis for the North Pacific Ocean (15°–70°N, 90°E–100°W). (a),(b) Percentage and the area-integrated explained variance for the first 10 EOFs over the region. (c)–(h) (top) The spatial structure of the EOF and the frequency power spectrum of the principal component (PC) time series of the corresponding EOF and (bottom) the first EOF for each model resolution and also an additional EOF selected to emphasize a mode that is qualitatively different from EOF1. Contours for the EOF maps in (c)–(h) are saturated at values ±(1/2)max|EOF|.

with patterns both in the Gulf Stream region and in the higher latitudes of the Labrador Sea, where the 0.25° model is not adequate to resolve eddies.[3] It is also interesting to note that the frequency power spectrum of the dominant EOFs shows a shift toward lower frequencies as we increase model resolution. Therefore, this analysis demonstrates that the dominant effect of improving model resolution in the North Atlantic is to focus low-frequency variability in eddying regions and to lengthen the time scale of that variability.

In the North Pacific, substantial differences in the EOF patterns between the 1° model and the higher-resolution models are found once again. The EOFs of the 1° model emerge as planetary waves traveling across the Pacific, while the higher-resolution models show patterns associated with the Kuroshio. The eddy-rich 0.1° model shows patterns of variability with nonzonal character compared with the eddy-present 0.25° model. Again, the frequency power spectrum of the principal components shows a shift toward lower frequencies for the eddy-rich model compared with the eddy-present model. Furthermore, the spectral peak in Figs. 5e and 5h is between 15 and 25 years.

The patterns of variability in the Indian Ocean for the 1° model with parameterized eddies are planetary waves, while

---

[3] The first baroclinic Rossby radius of deformation decreases as we move poleward, and, consequently, this results in smaller typical sizes for eddies closer to the poles (Hallberg 2013).

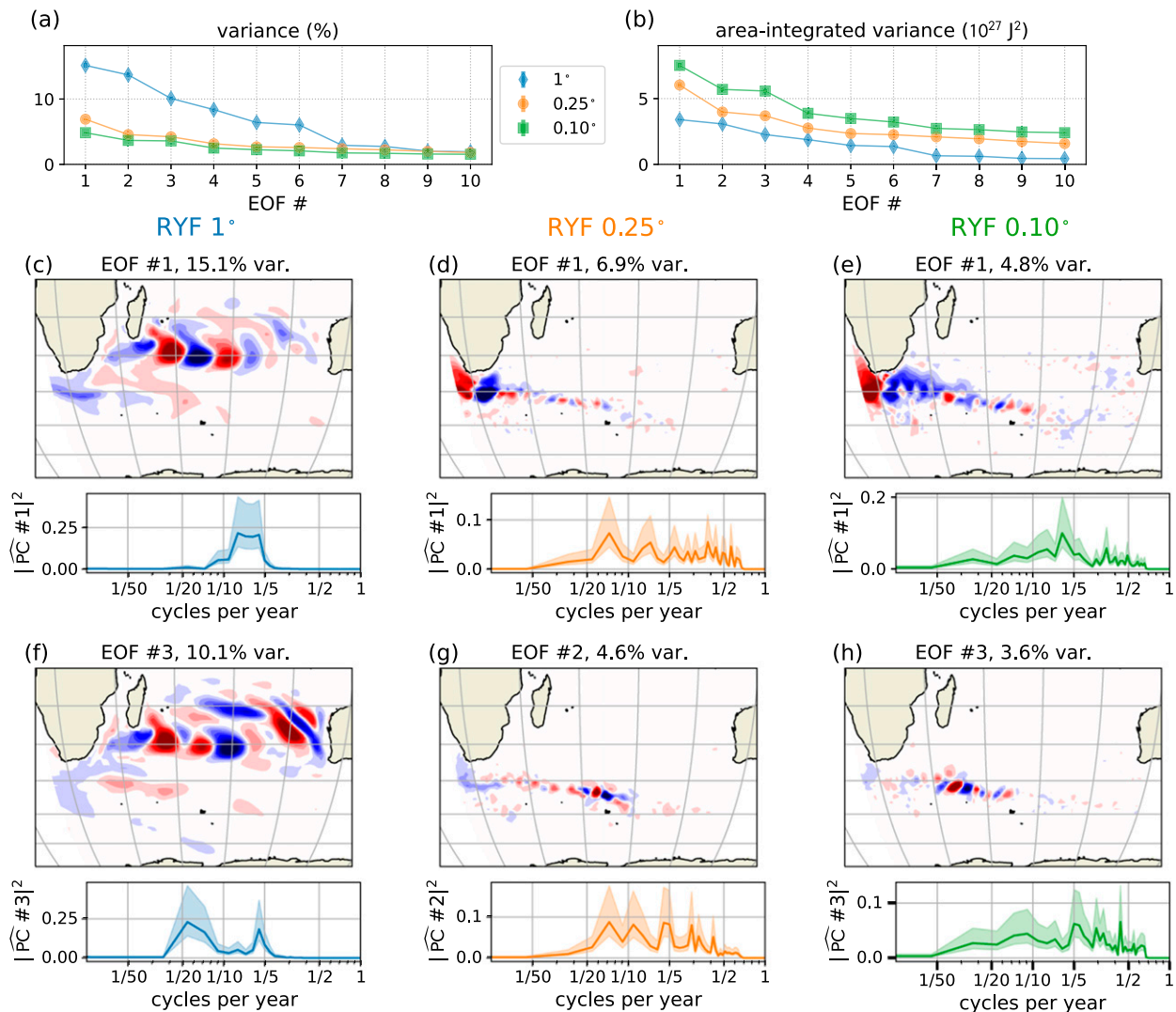EOF analysis of Indian Ocean

FIG. 6. Regional EOF analysis for the Indian Ocean (10°–70°S, 5°–120°E). (a),(b) Percentage and the area-integrated explained variance for the first 10 EOFs over the region. (c)–(h) (top) The spatial structure of the EOF and the frequency power spectrum of the principal component (PC) time series of the corresponding EOF and (bottom) the first EOF for each model resolution and also an additional EOF selected to emphasize a mode that is qualitatively different from EOF1. Contours for the EOF maps in (c)–(h) are saturated at values ±(1/2)max|EOF|.

the patterns for the higher-resolution models seem to be associated with the Agulhas retroflection and the Southern Ocean fronts (Fig. 6). Long baroclinic Rossby wave patterns, similar to those seen in the subtropical Indian Ocean for the 1° model (Figs. 6c,f) and at the same location, dominate the variability in a 1° resolution coupled climate model (Wolfe et al. 2017; Chapman et al. 2020). That we find these patterns emerging out of the EOF analysis of the repeat-year forced ocean–sea ice model, argues that these long baroclinic Rossby waves are, at least to some extent, a result of the ocean's intrinsic variability rather than from the coupled ocean–atmosphere interaction. We were not able, however, to see similar patterns emerging in the higher-resolution

repeat-year-forced models (RYF 0.25° and 0.10°) in the first 30 EOFs. This result suggests that at least the intrinsic oceanic component of the long baroclinic waves discussed by Wolfe et al. (2017) and Chapman et al. (2020) is a feature of models with resolution that require oceanic eddies to be parameterized.

Another feature of Fig. 6 is the similarity between the EOF patterns at eddy-present and eddy-rich resolutions. In both cases, the primary mode of variability is a broadband mode that manifests in variations in the zonal position of the Agulhas retroflection. The other mode shown in Figs. 6g and 6h reveals lower-frequency variability in the meander downstream of the Agulhas region. The similarity of these patterns suggests
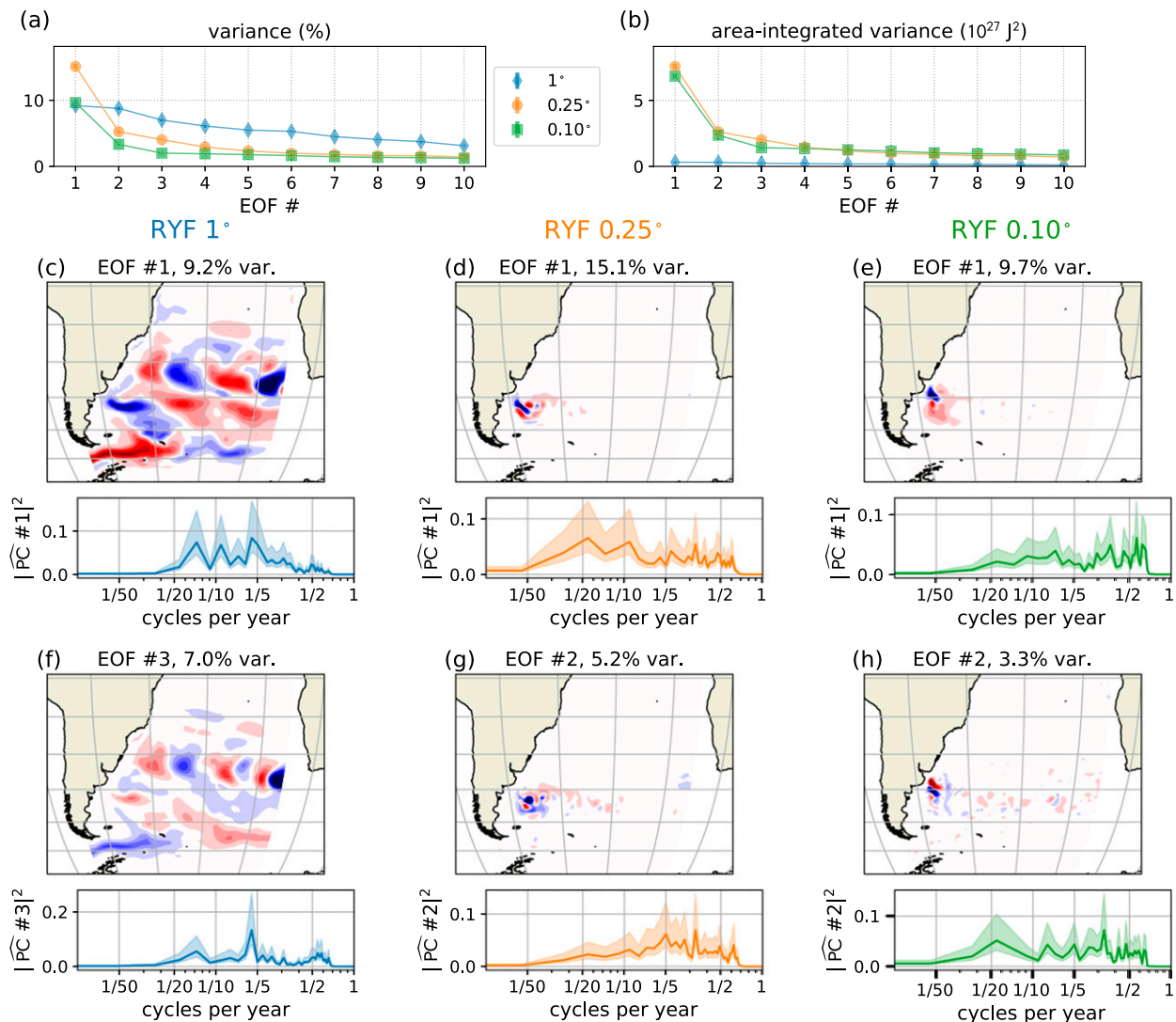
EOF analysis of South Atlantic

FIG. 7. Regional EOF analysis for the South Atlantic Ocean (10°–75°S, 70°W–10°E). (a),(b) Percentage and the area-integrated explained variance for the first 10 EOFs over the region. (c)–(h) (top) The spatial structure of the EOF and the frequency power spectrum of the principal component (PC) time series of the corresponding EOF and (bottom) the first EOF for each model resolution and also an additional EOF selected to emphasize a mode that is qualitatively different from EOF1. Contours for the EOF maps in (c)–(h) are saturated at values ±(1/2)max|EOF|.

that 0.25° resolution may be sufficient to represent the primary modes of low-frequency variability in this region.

Last, the EOF analysis in the South Atlantic Ocean region (Fig. 7) argues that the main pattern of variability is related to the Malvinas Current region, with the higher-resolution models showing a tendency for a peak of the principal component power spectrum at longer time scales. For the 1° model, the low-frequency variance is almost negligible (Fig. 7b) and, once again, planetary-wave patterns dominate the variability.

The North Pacific, South Atlantic, and Indian Ocean EOF analyses reveal striking differences between the 1° model with parameterized ocean eddies and the other two resolutions. In

these regions, the explained variance of the 1° is less than the eddy-present/eddy-rich models. The 1° EOFs show wavelike patterns, which may be a signature of baroclinic Rossby waves (see, e.g., Fig. 5c). On the other hand, when eddies are at least partially resolved, these long waves are replaced with patterns that mirror the eddy effect on large-scale circulation patterns (e.g., the Kuroshio in Fig. 5e).

4. Discussion

The ocean's larger heat capacity, compared with that of the atmosphere, is commonly viewed as the cause of the ocean

acting as an "integrator" for atmospheric high-frequency synoptic variability, reddening the power spectrum of motions—in other words, enhancing power at low frequencies, that is with decadal time scales (null hypothesis; Hasselmann 1976; Frankignoul and Hasselmann 1977). In this work, we investigated whether the ocean's intrinsic dynamics, which give rise to the rich high-frequency mesoscale and submesoscale oceanic eddy features, can further enhance the low-frequency variability of the ocean. In particular, we have focused on whether higher-resolution ocean simulation show differences in the low-frequency variability of the upper-ocean heat content at length scales comparable to or larger than the typical scales of atmospheric variability. Such low-frequency patterns of upper-ocean heat content may directly feed back on the atmosphere, give rise to decadal modes of climate variability, and therefore potentially affect global climate.

We have assessed the effect of the intrinsic oceanic variability using a global ocean–sea ice model at three different resolutions: eddy-rich 0.10°, eddy-present 0.25°, and with parameterized eddies at 1°. To disentangle the forced from the intrinsic component of ocean's variability, we used two different forcing schemes: (i) interannually varying forcing (IAF) from the JRA55-do atmospheric dataset for 1958–2018 and (ii) repeat-year forcing (RYF) from May 1990 to April 1991 from the JRA55-do. Since the RYF does not force any time scales longer than 1 year, it allows us to directly probe the ocean's intrinsic variability at decadal time scales. We have used two fields to investigate large-scale, low-frequency patterns of intrinsic ocean variability: the upper-ocean heat content (top 50 m of the ocean) and the sea surface height. The sea surface height served as a proxy for upper-ocean heat content and further allowed us to ground truth our model results against observations from the satellite altimetry record. Despite the short length of the altimetry record (27 years), which does not capture well the decadal variability, the comparison of the low-frequency variance from the interannually forced eddy-rich model (0.10°) model with that from the observations is encouraging (see Figs. 1g,j,k).

Our results demonstrate that (i) models that resolve eddies have much more variance of the upper-ocean heat content at decadal time scales (section 3a) and, furthermore, (ii) the spatial patterns of the low-frequency variability of upper-ocean heat content are limited in models that rely on eddy parameterizations (see section 3b). The direct effect of the intrinsic ocean dynamics on the low-frequency variability of upper-ocean heat content is negligible in the tropical regions but it is particularly pronounced in the extratropics, where the ocean's mesoscale is most active (see Figs. 1 and 2). Eddy-resolving models not only show enhanced low-frequency variance but, furthermore, EOF analysis reveals that the main modes of variability have patterns that are aligned with nonlinear flow structures, rather than baroclinic waves or spurious convection. Last, variability occurs at lower frequencies in higher-resolution models.

The differences in the low-frequency variability across model resolutions could be attributed either to changes on the mean states that the models show (e.g., mean currents or mean stratification) or to dynamical processes that are enabled with higher resolution. The mean state of these models across 1°, 0.25°, and 0.10° resolution is not substantially different (Kiss et al. 2020) (except, of course, in the Labrador Sea region where the 1° models show spurious convection). We, therefore, argue that the most likely candidates to explain the changes in the patterns and the changes in the time scales of the low-frequency variability we observe are eddy–mean flow interactions (as, for example, the case of the turbulent oscillator; Berloff et al. 2007), wave–eddy interactions (Sérazin et al. 2018), or eddy–eddy interactions.

The above-mentioned results may be used to infer a role for the extratropical ocean in generating modes of low-frequency climate variability such as the North Atlantic Oscillation (NAO; Hurrell et al. 2001) or the interdecadal Pacific oscillation (IPO; Mantua and Hare 2002). For example, in the Pacific Ocean, the time scale of dominant modes of variability for the eddy-rich model at 0.10° is between 10 and 20 years (see Figs. 5e, h), which is similar to the time scale of the IPO. Recent Earth system simulations revealed that the IPO is in better agreement with observations in simulations with higher lateral resolution (Chang et al. 2020). The IPO is a much broader pattern of variability than the EOF patterns we see in Fig. 5. However, a viable hypothesis may be that intrinsic oceanic variability in the extratropics could be amplified at the surface by ocean–atmosphere feedback mechanisms such as the wind–evaporation–sea surface temperature feedback (Xie and Philander 1994) and conveyed to the tropics through dynamics known as Pacific meridional modes (Alexander et al. 2010; Di Lorenzo et al. 2015; Amaya 2019). Once they propagate into the tropics these sea surface temperature anomalies can modulate ENSO dynamics at interdecadal frequencies and feed back to the extratropics via ENSO teleconnections (Newman et al. 2003; Alexander et al. 2002), hence explaining the broader signature of the main low-frequency mode of variability of the Pacific Ocean, the IPO. In summary, the results we presented in this paper argue that (i) that oceanic dynamics are largely responsible for the better agreement compared to observations seen in higher-resolution simulations and (ii) we further speculate that the extratropical oceans may provide the low-frequency trigger that might help to explain the IPO.

In view of the discussion above, we conclude that resolving the oceanic eddies in the eddy-active regions, and thus better capturing the low-frequency variability induced by intrinsic ocean dynamics in the extratropics, has global implications for modeling decadal variability and hence decadal predictions and climate projections. These results may have ramifications for our interpretation of model output and, in turn, affect future climate predictions. The large majority of CMIP6 climate models used for climate projections have an ocean component with a 1° resolution that is too coarse to resolve ocean eddies. Our results, thus, suggest that in those CMIP6 climate models, the ocean's input to atmospheric variability is weaker (cf. Figs. 2b and 2h) and also has different spatial patterns than when eddies are represented; for example, compare Figs. 3c,e with Figs. 3e,h. Correctly capturing these large-scale, low-frequency patterns of variability that force

FIG. 8. Sean R. Haney; February 1987–January 2021.

the atmosphere is crucial not only for predicting climate modes of variability at decadal time scales (El Niño, interdecadal Pacific oscillation, North Atlantic Oscillation, Indian Ocean dipole) but also for future climate predictions. Our results suggest the imperative for moving toward coupled climate models with an ocean component with, at least, an eddy-present lateral resolution.

APPENDIX

EOF Analysis: Error Bars and Robustness

The standard error of the EOF analysis eigenvalues is computed using the criterion by North et al. (1982). This standard error is shown in both panels (a) and (b) in Figs. 3–7. It is generally small enough to be barely distinguishable over the marker size.

For the power spectra shown in panels (c) to (h) in Figs. 3–7, we split the principal component time series into four consecutive segments (55 years long at least) and then computed the mean power spectrum of each segment. The error bars were obtained using the χ^2 criterion with a 95% confidence interval.

The robustness of the spatial patterns of the EOF analysis was checked by comparing the patterns of EOF analysis from (i) full times series, (ii) the first 60% of the time series, and (iii) the last 60% of the time series. For the regions presented here we, typically, find that the EOF patterns 1 and 2 were found to be the same. Sometimes EOF patterns 3–5 come in different order (e.g., what was EOF3 using the full time series could be EOF4 when using the first 60% of the time series).

Jupyter notebooks that reproduce the EOF-analysis sensitivity tests can be found at the GitHub repository https://github.com/navidcy/IntrinsicOceanicLFVariabilityUOHC.

REFERENCES

Alexander, M. A., I. Bladé, M. Newman, J. R. Lanzante, N.-C. Lau, and J. D. Scott, 2002: The atmospheric bridge: The influence of ENSO teleconnections on air–sea interaction over the global oceans. *J. Climate*, **15**, 2205–2231, https://doi.org/10.1175/1520-0442(2002)015<2205:TABTIO>2.0.CO;2.

——, D. J. Vimont, P. Chang, and J. D. Scott, 2010: The impact of extratropical atmospheric variability on ENSO: Testing the seasonal footprinting mechanism using coupled model experiments. *J. Climate*, **23**, 2885–2901, https://doi.org/10.1175/2010JCLI3205.1.

Amaya, D. J., 2019: The Pacific Meridional Mode and ENSO: A review. *Curr. Climate Change Rep.*, **5**, 296–307, https://doi.org/10.1007/s40641-019-00142-x.

Aoki, K., Y. Miyazawa, T. Hihara, and T. Miyama, 2020: An objective method for probabilistic forecasting of multimodal

Kuroshio states using ensemble simulation and machine learning. *J. Phys. Oceanogr.*, **50**, 3189–3204, https://doi.org/10.1175/JPO-D-19-0316.1.

Barsugli, J. J., and D. S. Battisti, 1998: The basic effects of atmosphere–ocean thermal coupling on midlatitude variability. *J. Atmos. Sci.*, **55**, 477–493, https://doi.org/10.1175/1520-0469(1998)055<0477:TBEOAO>2.0.CO;2.

Berloff, P. S., A. M. Hogg, and W. Dewar, 2007: The turbulent oscillator: A mechanism of low-frequency variability of the wind-driven ocean gyres. *J. Phys. Oceanogr.*, **37**, 2363–2386, https://doi.org/10.1175/JPO3118.1.

Bishop, S. P., R. J. Small, F. O. Bryan, and R. A. Tomas, 2017: Scale dependence of midlatitude air–sea interaction. *J. Climate*, **30**, 8207–8221, https://doi.org/10.1175/JCLI-D-17-0159.1.

Bouchet, F., J. Rolland, and E. Simonnet, 2019: Rare event algorithm links transitions in turbulent flows with activated nucleations. *Phys. Rev. Lett.*, **122**, 074502, https://doi.org/10.1103/PhysRevLett.122.074502.

Bryan, F. O., R. Tomas, J. M. Dennis, D. B. Chelton, N. G. Loeb, and J. L. McClean, 2010: Frontal scale air–sea interaction in high-resolution coupled climate models. *J. Climate*, **23**, 6277–6291, https://doi.org/10.1175/2010JCLI3665.1.

Buckley, M. W., R. M. Ponte, G. Forget, and P. Heimbach, 2014: Low-frequency SST and upper-ocean heat content variability in the North Atlantic. *J. Climate*, **27**, 4996–5018, https://doi.org/10.1175/JCLI-D-13-00316.1.

——, ——, ——, and ——, 2015: Determining the origins of advective heat transport convergence variability in the North Atlantic. *J. Climate*, **28**, 3943–3956, https://doi.org/10.1175/JCLI-D-14-00579.1.

Chang, P., and Coauthors, 2020: An unprecedented set of high-resolution Earth system simulations for understanding multiscale interactions in climate variability and change. *J. Adv. Model. Earth Syst.*, **12**, e2020MS002298, https://doi.org/10.1029/2020MS002298.

Chapman, C. C., B. M. Sloyan, T. J. O'Kane, and M. A. Chamberlain, 2020: Interannual subtropical Indian Ocean variability due to long baroclinic planetary waves. *J. Climate*, **33**, 6765–6791, https://doi.org/10.1175/JCLI-D-19-0469.1.

Constantinou, N. C., 2015: Formation of large-scale structures by turbulence in rotating planets. Ph.D. thesis, National and Kapodistrian University of Athens, 190 pp., http://www.didaktorika.gr/eadd/handle/10442/35501?locale=en.

——, B. F. Farrell, and P. J. Ioannou, 2014: Emergence and equilibration of jets in beta-plane turbulence: Applications of stochastic structural stability theory. *J. Atmos. Sci.*, **71**, 1818–1842, https://doi.org/10.1175/JAS-D-13-076.1.

Dawson, A., 2016: eofs: A library for EOF analysis of meteorological, oceanographic, and climate data. *J. Open Res. Softw.*, **4**, e14.

Deshayes, J., and Coauthors, 2013: Oceanic hindcast simulations at high resolution suggest that the Atlantic MOC is bistable. *Geophys. Res. Lett.*, **40**, 3069–3073, https://doi.org/10.1002/grl.50534.

Di Lorenzo, E., G. Liguori, N. Schneider, J. C. Furtado, B. T. Anderson, and M. A. Alexander, 2015: ENSO and meridional modes: A null hypothesis for Pacific climate variability. *Geophys. Res. Lett.*, **42**, 9440–9448, https://doi.org/10.1002/2015GL066281.

Farrell, B. F., and P. J. Ioannou, 2008: Formation of jets by baroclinic turbulence. *J. Atmos. Sci.*, **65**, 3353–3375, https://doi.org/10.1175/2008JAS2611.1.

——, and ——, 2019: Statistical state dynamics: A new perspective on turbulence in shear flow. *Zonal Jets: Phenomenology,*

Genesis, and Physics, B. Galperin and P. L. Read, Eds., Cambridge University Press, 380–400, https://doi.org/10.1017/9781107358225.025.

Frankignoul, C., and K. Hasselmann, 1977: Stochastic climate models. Part II. Application to sea-surface temperature anomalies and thermocline variability. *Tellus*, **29**, 289–305, https://doi.org/10.3402/tellusa.v29i4.11362.

Hallberg, R., 2013: Using a resolution function to regulate parameterizations of oceanic mesoscale eddy effects. *Ocean Modell.*, **72**, 92–103, https://doi.org/10.1016/j.ocemod.2013.08.007.

Hasselmann, K., 1976: Stochastic climate models Part I. Theory. *Tellus*, **28**, 473–485, https://doi.org/10.3402/tellusa.v28i6.11316.

Hewitt, H. T., and Coauthors, 2020: Resolving and parameterising the ocean mesoscale in Earth system models. *Curr. Climate Change Rep.*, **6**, 137–152, https://doi.org/10.1007/s40641-020-00164-w.

Hogg, A. M., P. D. Killworth, J. R. Blundell, and W. K. Dewar, 2005: Mechanisms of decadal variability of the wind-driven ocean circulation. *J. Phys. Oceanogr.*, **35**, 512–531, https://doi.org/10.1175/JPO2687.1.

——, W. K. Dewar, P. D. Killworth, and J. R. Blundell, 2006: Decadal variability of the midlatitude climate system driven by the ocean circulation. *J. Climate*, **19**, 1149–1166, https://doi.org/10.1175/JCLI3651.1.

Hoyer, S., and J. Hamman, 2017: xarray: N-D labeled arrays and datasets in Python. *J. Open Res. Softw.*, **5**, 10, https://doi.org/10.5334/jors.148.

Hurrell, J. W., Y. Kushnir, and M. Visbeck, 2001: The North Atlantic oscillation. *Science*, **291**, 603–605, https://doi.org/10.1126/science.1058761.

Hyder, P., and Coauthors, 2018: Critical Southern Ocean climate model biases traced to atmospheric model cloud errors. *Nat. Commun.*, **9**, 3625, https://doi.org/10.1038/s41467-018-05634-2.

James, I. N., 1998: Internal and external variability in a baroclinic atmosphere. *Dyn. Atmos. Oceans*, **27**, 351–359, https://doi.org/10.1016/S0377-0265(97)00018-3.

——, and P. M. James, 1992: Spatial structure of ultra-low-frequency variability of the flow in a simple atmospheric circulation model. *Quart. J. Roy. Meteor. Soc.*, **118**, 1211–1233, https://doi.org/10.1002/qj.49711850810.

Kimoto, M., and M. Ghil, 1993: Multiple regimes in the Northern Hemisphere winter. Part I: Methodology and hemispheric regimes. *J. Atmos. Sci.*, **50**, 2625–2643, https://doi.org/10.1175/1520-0469(1993)050<2625:MFRITN>2.0.CO;2.

Kiss, A. E., and Coauthors, 2020: ACCESS-OM2 v1.0: A global ocean-sea ice model at three resolutions. *Geosci. Model Dev.*, **13**, 401–442, https://doi.org/10.5194/gmd-13-401-2020.

Leroux, S., T. Penduff, L. Bessières, J. M. Molines, J. M. Brankart, G. Sérazin, B. Barnier, and L. Terray, 2018: Intrinsic and atmospherically forced variability of the AMOC: Insights from a large-ensemble ocean hindcast. *J. Climate*, **31**, 1183–1203, https://doi.org/10.1175/JCLI-D-17-0168.1.

Mantua, N. J., and S. R. Hare, 2002: The Pacific decadal oscillation. *J. Oceanogr.*, **58**, 35–44, https://doi.org/10.1023/A:1015820616384.

Martin, P. E., B. K. Arbic, A. M. Hogg, A. E. Kiss, J. R. Munroe, and J. R. Blundell, 2020: Frequency-domain analysis of the energy budget in an idealized coupled ocean–atmosphere model. *J. Climate*, **33**, 707–726, https://doi.org/10.1175/JCLI-D-19-0118.1.

——, ——, and ——, 2021: Drivers of atmospheric and oceanic surface temperature variance: A frequency domain approach.

J. Climate, **34**, 4603–4624, https://doi.org/10.1175/JCLI-D-20-0636.1.

Newman, M., G. P. Compo, and M. A. Alexander, 2003: ENSO-forced variability of the Pacific decadal oscillation. *J. Climate*, **16**, 3853–3857, https://doi.org/10.1175/1520-0442(2003)016<3853:EVOTPD>2.0.CO;2.

North, G. R., T. L. Bell, R. F. Cahalan, and F. J. Moeng, 1982: Sampling errors in the estimation of empirical orthogonal functions. *Mon. Wea. Rev.*, **110**, 699–706, https://doi.org/10.1175/1520-0493(1982)110<0699:SEITEO>2.0.CO;2.

Ortega, P., J. Robson, R. T. Sutton, and M. B. Andrews, 2017: Mechanisms of decadal variability in the Labrador Sea and the wider North Atlantic in a high-resolution climate model. *Climate Dyn.*, **49**, 2625–2647, https://doi.org/10.1007/s00382-016-3467-y.

Parker, J. B., and J. A. Krommes, 2013: Zonal flow as pattern formation. *Phys. Plasmas*, **20**, 100703, https://doi.org/10.1063/1.4828717.

Penduff, T., M. Juza, B. Barnier, J. Zika, W. K. Dewar, A.-M. Treguier, J.-M. Molines, and N. Audiffren, 2011: Sea level expression of intrinsic and forced ocean variabilities at interannual time scales. *J. Climate*, **24**, 5652–5670, https://doi.org/10.1175/JCLI-D-11-00077.1.

——, and Coauthors, 2018: Chaotic variability of ocean heat content: Climate-relevant features and observational implications. *Oceanography*, **31**, 63–71, https://doi.org/10.5670/oceanog.2018.210.

Pierini, S., 2006: A Kuroshio Extension system model study: Decadal chaotic self-sustained oscillations. *J. Phys. Oceanogr.*, **36**, 1605–1625, https://doi.org/10.1175/JPO2931.1.

——, H. A. Dijkstra, and A. Riccio, 2009: A nonlinear theory of the Kuroshio Extension bimodality. *J. Phys. Oceanogr.*, **39**, 2212–2229, https://doi.org/10.1175/2009JPO4181.1.

Qiu, B., and W. Miao, 2000: Kuroshio path variations south of Japan: Bimodality as a self-sustained internal oscillation. *J. Phys. Oceanogr.*, **30**, 2124–2137, https://doi.org/10.1175/1520-0485(2000)030<2124:KPVSOJ>2.0.CO;2.

——, and S. Chen, 2010: Eddy–mean flow interaction in the decadally modulating Kuroshio Extension system. *Deep-Sea Res. II*, **57**, 1098–1110, https://doi.org/10.1016/j.dsr2.2008.11.036.

Rocklin, M., 2015: Dask: Parallel computation with blocked algorithms and task scheduling. *Proc. SciPy 2015: 14th Python in Sci. Conf.*, Austin, TX, SciPy.org, 130–136, https://doi.org/10.25080/Majora-7b98e3ed-013.

Sérazin, G., T. Penduff, S. Grégorio, B. Barnier, J.-M. Molines, and L. Terray, 2015: Intrinsic variability of sea level from global ocean simulations: Spatiotemporal scales. *J. Climate*, **28**, 4279–4292, https://doi.org/10.1175/JCLI-D-14-00554.1.

——, and Coauthors, 2017: A global probabilistic study of the ocean heat content low-frequency variability: Atmospheric

forcing versus oceanic chaos. *Geophys. Res. Lett.*, **44**, 5580–5589, https://doi.org/10.1002/2017GL073026.

——, T. Penduff, B. Barnier, J.-M. Molines, B. K. Arbic, M. Müller, and L. Terray, 2018: Inverse cascades of kinetic energy as a source of intrinsic variability: A global OGCM study. *J. Phys. Oceanogr.*, **48**, 1385–1408, https://doi.org/10.1175/JPO-D-17-0136.1.

Simonnet, E., J. Rolland, and F. Bouchet, 2021: Multistability and rare spontaneous transitions in barotropic β-plane turbulence. *J. Atmos. Sci.*, **78**, 1889–1911, https://doi.org/10.1175/JAS-D-20-0279.1.

Small, R. J., F. O. Bryan, S. P. Bishop, and R. A. Tomas, 2019: Air–sea turbulent heat fluxes in climate models and observational analyses: What drives their variability? *J. Climate*, **32**, 2397–2421, https://doi.org/10.1175/JCLI-D-18-0576.1.

——, ——, ——, S. Larson, and R. A. Tomas, 2020: What drives upper-ocean temperature variability in coupled climate models and observations? *J. Climate*, **33**, 577–596, https://doi.org/10.1175/JCLI-D-19-0295.1.

Stewart, K., and Coauthors, 2020: JRA55-do-based repeat year forcing datasets for driving ocean–sea-ice models. *Ocean Modell.*, **147**, 101557, https://doi.org/10.1016/j.ocemod.2019.101557.

Timmermann, A., and Coauthors, 2018: El Niño–Southern Oscillation complexity. *Nature*, **559**, 535–545, https://doi.org/10.1038/s41586-018-0252-6.

Tsujino, H., and Coauthors, 2018: JRA-55 based surface dataset for driving ocean–sea-ice models (JRA55-do). *Ocean Modell.*, **130**, 79–139, https://doi.org/10.1016/j.ocemod.2018.07.002.

Uchida, T., and Coauthors, 2020: xrft: v0.2.1. Zenodo, https://doi.org/10.5281/zenodo.4022471.

Vallis, G. K., 2010: Mechanisms of climate variability from years to decades. *Stochastic Physics and Climate Modelling*, T. N. Palmer and P. Williams, Eds., Cambridge University Press, 1–34.

Webster, P. J., A. M. Moore, J. P. Loschnigg, and R. R. Leben, 1999: Coupled ocean–atmosphere dynamics in the Indian Ocean during 1997–98. *Nature*, **401**, 356–360, https://doi.org/10.1038/43848.

Wolfe, C. L., P. Cessi, and B. D. Cornuelle, 2017: An intrinsic mode of interannual variability in the Indian Ocean. *J. Phys. Oceanogr.*, **47**, 701–719, https://doi.org/10.1175/JPO-D-16-0177.1.

Xie, S.-P., and S. G. H. Philander, 1994: A coupled ocean–atmosphere model of relevance to the ITCZ in the eastern Pacific. *Tellus*, **46A**, 340–350, https://doi.org/10.3402/tellusa.v46i4.15484.

Zhuang, J., and Coauthors, 2020: xesmf: v0.5.2. Zenodo, https://doi.org/10.5281/zenodo.3700105.